Dimerization of iLID Optogenetic Proteins Observed Using 3D Single-Molecule Tracking in Live Bacterial Cells

Alecia M. Achimovich[a], Ting Yan[b] and Andreas Gahlmann[a,b#]

[a]Department of Molecular Physiology & Biological Physics, University of Virginia School of Medicine, Charlottesville, Virginia, USA

[b]Department of Chemistry, University of Virginia, Charlottesville, Virginia

#Address correspondence to Andreas Gahlmann, agahlmann@virginia.edu

ABSTRACT

3D single molecule tracking microscopy has enabled measurements of protein diffusion in living cells, offering information about protein dynamics and the cellular environment. For example, different diffusive states can be resolved and assigned to protein complexes of different size and composition. However, substantial statistical power and biological validation, often through genetic deletion of binding partners, are required to support diffusive state assignments. When investigating some cellular processes, transient perturbation to protein spatial distributions is preferable to permanent genetic deletion of an essential protein. Optogenetic dimerization systems can be used to manipulate protein spatial distributions which could offer a means to deplete specific diffusive states observed in single molecule tracking experiments. Here, we evaluate the performance of the iLID optogenetic system in living *E. coli* cells using diffraction-limited microscopy and 3D single molecule tracking. We observed a robust optogenetic response in protein spatial distribution after 488 nm laser activation. Surprisingly, 3D single molecule tracking results indicate activation of the optogenetic response at high intensity wavelengths for which there is evidence of minimal photon absorbance by the LOV2 domain. However, the preactivation response was minimized through the use of iLID system mutants, and titration of protein expression levels.

INTRODUCTION

Many fluorescence microscopy-based techniques have been developed over the past decades to detect and quantify interactions between biomolecules *in vitro* and *in vivo*. Improvements of fluorescent probes and biomolecular labeling technologies in conjunction with instrumental improvements have enabled measurements that provide critical insights into cellular organization and the biochemical interactions occurring within them.[1] Spatial co-localization of emitters through multi-color imaging has been widely utilized to gauge whether biomolecules are close in space and are thus able to interact. The power of such measurements depends critically on the achievable spatial resolution of the instrument used. Diffraction-limited imaging provides 200-300 nm resolution, which is orders of magnitude larger than the size of a typical protein (~2 nm) or the size of small protein complexes (~20 nm). Diffraction-limited resolution is thus too low to conclusively determine whether two proteins interact directly or whether their interaction is mediated by a third protein[2]. Super-resolution microscopy approaches such as PALM/STORM and MINFLUX, have been successful in addressing this challenge by enabling precise single-molecule localization with tens of nanometers of precision. For example, Symborska et al. determined radial positions of protein subunits of the nuclear pore complex (NPC) with subnanometer precision using PALM/STORM in conjunction with particle averaging[3]. This approach was later extended to achieve a 3D reconstruction of the nuclear pore complex through iterative multi-color imaging of each NPC subunit relative to a reference protein also within the NPC.[4] More recently, Ries and co-workers used MINFLUX microscopy to pinpoint the position of subunits within the NPC with single nanometer precision without the need for radial averaging[5]. Thus, for relatively large, immobile, and highly symmetric structures like the nuclear pore

complex, super-resolution fluorescence microscopy can provide accurate co-localization data that provides information on how individual subunits interact with each other.[6-8]

Detecting protein interactions within freely-diffusing complexes cannot be accomplished by fluorescence co-localization and thus requires different approaches. Live cell measurements of protein oligomerization is possible using fluorescence microscopy techniques such as Fluorescence recovery after photobleaching (FRAP), and Fluorescence correlation spectroscopy (FCS)[9-11]. These methods have gained popularity due to the increased availability of commercial confocal laser scanning microscopes over the past twenty years. Because they provide complimentary measurements, FCS and FRAP can be used together to probe binding kinetics of protein-protein interactions[12,13]. However, it is difficult to identify transient binding events from these data because these methods provide ensemble-averaged data. Alternatively, Forster resonance energy transfer (FRET), measures the efficiency of non-radiative energy transfer from an excited donor fluorophore to an acceptor fluorophore in the ground state over a distance of a few nanometers[14,15]. Thus, FRET efficiency serves as a measurement of spatial proximity of fluorescently labeled proteins and can be used to infer protein-protein interactions.

Detecting interactions of diffusing proteins using dual-color single-molecule microscopy is not practically feasible because both fluorophores used to label the putative interacting proteins must be in a fluorescent ON state at the same time within the same complex. The probability of observing such co-diffusion directly in separate color-channels is negligibly small, because fluorophore photo-activation or blinking in PALM/STORM occurs stochastically. To avoid this problem, the diffusive behaviors of putative interacting proteins can be measured in separate experiments. If the two proteins diffuse at the same rate, then it is possible that they exist within the same protein complex. Because single-molecule trajectories in living cells are limited in

duration by fluorophore photobleaching, information from thousands of trajectories are often pooled and statistical data analysis approaches are employed to resolve different diffusive states[16-23]. Indeed, different diffusive states can be resolved in living cells due to homo- and heterooligomeric complex formation among interacting proteins[23-25] or proteins binding to quasi-stationary structures, such as DNA[26-36]. However, to assign diffusive states to specific biomolecular complexes of different protein compositions, additional experimental perturbation is needed. Single-point mutations or genetic deletion mutants of potential interacting partners can be used as a tool to disrupt putative complexes and observe changes in diffusive behavior. A drawback of such genetic approaches is that the permanent disruption of an interaction interface or absence of a binding partner can interfere with cellular processes in ways that are difficult to predict or control, or yield the cells inviable[37,38]. Therefore, controllable, transient perturbations of cellular processes on experimentally-relevant time scales is preferable.

Optically and chemically induced dimerization provides a favorable alternative to permanent genetic perturbations. Such optogenetic and chemogenetic dimerization systems enable manipulation of protein spatial localization in so-called knocksideways assays[39,40]. In a knocksideways experiment, one of the dimerizing molecules is attached to a cytosolic protein of interest and the other dimerization partner is targeted to a cellular location that differs from the native localization of the tagged protein of interest (e.g. the cell membrane). Upon optical or chemical stimulation of dimerization, the protein of interest is sequestered away from its native localization, and interacting proteins can be sequestered along with it. Optogenetic knocksideways experiments can thus be used to detect molecular interactions in living cells.

We reasoned that manipulating the spatial distributions of otherwise cytosolic proteins would aid the assignment of diffusive states (observed in single-molecule tracking experiments)

to protein complexes of specific protein composition. In the simplest scenario, depletion of the cytosolic diffusive state corresponding to the suspected oligomer would be expected when either interacting partner is sequestered to the membrane. Chemogenetic systems rely on dimerization being induced by a diffusing molecule itself, whereas optogenetic systems can be activated by photon absorption. Optogenetic systems thus allows for more precise spatial and temporal control over dimerization than chemogenetic systems.

Here, we test the possibility of combining optogenetic manipulation with 3D single-molecule tracking microscopy in live *Esherichia coli*. The improved Light Induced Dimerization (iLID) system[4] was selected because it has been extensively characterized and engineered for optimized performance in different model systems. Thus, a considerably large toolbox of iLID variants with different affinities, and reversion times are available for implementation[41-43]. The iLID protein contains the light sensing light oxygen voltage (LOV2) domain derived from *Avena sativa* which incorporates a flavin cofactor during folding. The flavin cofactor acts as a chromophore, and forms a cysteine adduct with the LOV2 domain after illumination with blue light. As a result, the iLID protein changes conformation and exposes a binding site for the interacting partner, SspB[44,45]. We demonstrate that the iLID system exhibits a robust response after 488 nm illumination in low-intensity excitation conditions used for diffraction-limited imaging. Using single-molecule tracking, we found that $SspB_{micro}$ exhibited the most substantial 488 nm-induced response among three tested SspB mutants. Surprisingly, our results also reveal that activation of the optogenetic response also occurs under high intensity illumination conditions, even at wavelengths for which iLID shows minimal absorbance. Titrating the iLID expression level with respect to SspB reduced imaging laser-induced iLID:SspB interaction in 3D single-

molecule tracking experiments Together our results establish the need for careful calibration of the optogenetic system prior to its application to imaging experiments.

RESULTS AND DISCUSSION

Diffraction-limited imaging indicates a robust redistribution of otherwise cytosolic fluorescence to the membrane upon blue-light activation.

Optogenetic tools have been widely applied in eukaryotic cells in conjunction with diffraction-limited fluorescence microscopy to obtain population-averaged, phenotypic readouts[46,47]. Therefore, we sought to quantify the optogenetic response of the iLID system in K12 *E.coli* using diffraction-limited imaging. We expressed the iLID protein from an inducible arabinose promoter and targeted it to the inner membrane using an N-terminal genetic fusion containing a modified single transmembrane spanning helix derived from the *E.coli* transmembrane protein, TatA[48,49]. This construct, herein referred to as MA-iLID, was previously used for stable insertion into the inner membrane of gram negative bacteria and has been shown to enable optogenetic disruption of type 3 protein secretion in *Yersinia enterocolitica.*[50]. We genetically fused the strongest reported iLID binding partner, $SspB_{nano}$, with a C-terminal Halo tag, and expressed this construct from a second, constitutively expressing plasmid. $SspB_{nano}$-Halo was labeled with JFX549 for visualization in fluorescence imaging experiments[51] (**Figure 1a**). For simplicity, the JFX549-labeled $SspB_{nano}$-Halo is referred to as $SspB_{nano}$ in this report.

Prior to optical activation of MA-iLID with 488 nm laser light, we observed a uniform distribution of cytosolic $SspB_{nano}$. Redistribution of $SspB_{nano}$ to the membrane was dependent on both expression of MA-iLID and 488 nm laser illumination (~1mW/cm^2) (**Figure 1b-d**). We quantified $SspB_{nano}$ redistribution upon 488 nm laser illumination in each cell using the structural similarity

index measure (SSIM), which quantifies similarity between two images[52]. Cells expressing MA-iLID were more dissimilar (1-SSIM) after 488 nm laser illumination compared to controls (**Figure 1e**). To estimate the fraction of molecules that reside at the membrane in each condition, we simulated 2D diffraction-limited images that matched our imaging parameters and contained realistic noise contributions (see methods) (**Figure 1f, SI Figure 1a**). Fluorescence line profiles across the midsection of cells showed a Gaussian-like line shape for cytosolic fluorescence, while membrane-associated fluorescence produced double-peaked line shapes. The experimental line shape obtained with a fluorescently labeled, membrane-anchored iLID protein (MA-mCherry-iLID) agreed well with line shape obtained based on simulated images of 100% membrane localized molecules (**SI Figure 1b**). Based on qualitative comparison of simulated and measured line shapes, we estimate that the fraction of molecules at the membrane in living cells is close to 0% pre-activation and greater than ~80% post-activation. These data suggest that the iLID system can be used to efficiently sequester otherwise cytosolic molecules to the membrane.

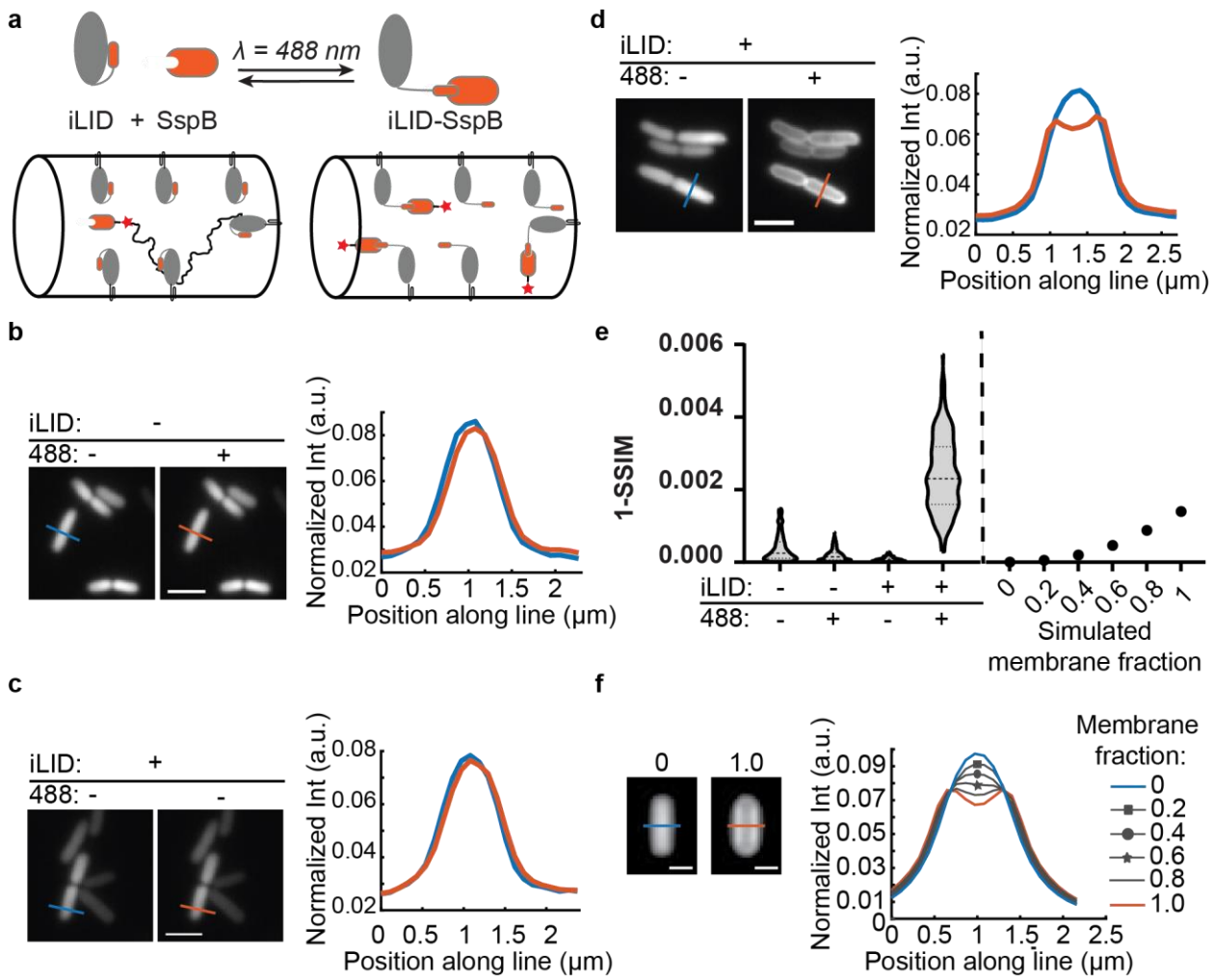

Figure 1. Diffraction-limited imaging indicates a substantial redistribution of $SspB_{nano}$ to the membrane after blue-light activation. (a) Schematic depiction of a knocksideways experiment using the iLID system. The iLID protein undergoes a conformational change after 488 nm-light illumination and uncages a binding site for SspB. Halo-tagged (red star) cytosolic SspB binds to membrane-anchored iLID (MA-iLID) after 488 nm illumination. SspB-Halo is labeled with JFX549 for fluorescence imaging (hereafter referred to as SspB). **(b)** Diffraction-limited images of $SspB_{nano}$. Illumination with 488 nm light has no effect on the spatial distribution of $SspB_{nano}$ in the absence of MA-iLID. Fluorescence intensity line profiles across the midsection of the cell (normalized to the integrated line intensity) also exhibit no apparent shift in $SspB_{nano}$ spatial distribution. **(c)** Low intensity (~1 W/cm^2) 561 nm laser excitation over the entire exposure (80 seconds) is not sufficient to induce $SspB_{nano}$ sequestration to the membrane. **(d)** In the presence of MA-iLID, low intensity (~4 mW/ cm^2) 488 nm laser illumination shifts the spatial distribution of $SspB_{nano}$ to the cell membrane. The fluorescence intensity line profile across the midsection of the cell changes from a Gaussian-like line shape to a characteristic double-peaked line shape. **(e)** Left panel: Image dissimilarity (1-SSIM) of experimentally-acquired individual cell images before and after 488 nm illumination (n=200-350 cells in each condition). A population-level response in image dissimilarity is dependent on MA-iLID expression and 488 nm illumination. Right panel: Calibration of the image dissimilarity metric as a function of the fraction of membrane-associated fluorophores (relative to a simulated cell with 0% membrane-associated fluorophores). **(f)**

Simulated diffraction limited images of cells with 0% or 100% membrane-associated fluorophores, respectively. Normalized line profiles of simulated diffraction-limited images (**SI Figure 1**) indicate a progressive broadening, and redistribution of fluorescence as the fraction of membrane-associated fluorophores increases.

3D single-molecule tracking data show increased SspB:iLID interaction prior to 488 nm illumination.

Single-molecule tracking microscopy has been used to resolve different diffusive states of proteins that manifest in living cells due to protein complex formation[53]. Because optical activation of the MA-iLID:SspB interaction allows for transient spatial redistribution of protein localization, the light-driven interaction could provide a means to non-invasively perturb the diffusive states that manifest in the cytosol of living cells. We therefore sought to measure SspB diffusive behavior in living cells and determine the extent of MA-iLID association using 3D single-molecule tracking. Based on the clear membrane localization of MA-iLID in diffraction limited images (SI Figure 1), we reasoned that $SspB_{nano}$ interacting with MA-iLID should diffuse along the membrane at a much slower rate than cytosolic $SspB_{nano}$. In 488 nm illuminated cells, the cumulative distribution function of apparent diffusion coefficients indeed shows a bimodal curve with a transition at $D^* = 0.15\ \mu m^2/s$ (**Figure 2a**). When plotting the spatial trajectories of slowly diffusing molecules ($D^* < 0.15\ \mu m^2/s$) it is clear that they localize near the bacterial membrane. On the other hand, the spatial trajectories of fast diffusing molecules ($D^* > 0.15\ um^2/s$) localize in the cytosol (**Figure 2b**). We conclude that it is possible to clearly distinguish freely-diffusing, cytosolic $SspB_{nano}$ from iLID-associated $SspB_{nano}$ molecules in living cells based on their diffusion rate and sub-cellular localization.

The $D^* = 0.15$ um^2/s threshold allowed us to estimate the relative population fractions of iLID-associated and cytosolic $SspB_{nano}$. In cells that do not express MA-iLID, the vast majority (95%) of $SspB_{nano}$ proteins diffuse fast and localize to the bacterial cytosol, as expected. The remaining 5% of tracked proteins were classified as slowly diffusing, but the corresponding trajectories showed no discernable preference for the membrane. The diffusive behavior and spatial distribution of $SspB_{nano}$ remained unchanged upon 488 nm illumination in these cells (**Figure 2a** and **c**). Surprisingly, and in contrast to the diffraction-limited images (**Figure 1**), a large fraction of $SspB_{nano}$ proteins exhibited slow diffusion (48%) in cells that express MA-iLID, even in the absence of 488 nm light. This shift towards slow diffusion is accompanied with spatial redistribution of $SspB_{nano}$ to the membrane, whereas the fast diffusing population of proteins remained uniformly localized to the cytosol (**Figure 2d**). When cells expressing both $SspB_{nano}$ and MA-iLID were exposed to 488 nm light, we observed an additional shift towards slower diffusion and membrane-proximal localization (56%) (**Figure 2e**). The increase in iLID-associated SspB observed is marginal compared to the shift observed in diffraction-limited images (**Figure 1**). However, we note that the line profile quantitation of our experimental images represents an example of a single cell displaying an obvious change in $SspB_{nano}$ spatial distribution. Across a population the degree of response observed in line profiles varies. Further, the population level analysis of image dissimilarity performed on the diffraction limited images indicates a varied response to 488 nm illumination. This is likely due to expression level heterogeneity which is evident in whole cell fluorescence comparisons of both arabinose-promoter driven expression of MA-iLID, and constitutive expression of SspB (**Figure 1, SI Figure 1**).

We hypothesize that the discrepancy of MA-iLID associated SspB seen in diffraction-limited image quantitation compared to single-molecule trajectory data is due to the higher

excitation intensity required for single-molecule localization microscopy. The absorption spectrum of iLID proteins shows very minimal absorption at wavelengths larger than 500 nm[54]. However, optical activation of the iLID:$SspB_{nano}$ interaction is possible with 514 nm light at illumination intensities typical for diffraction-limited imaging (~1 W/cm^2). (**SI Figure 2**). The intensity used for JFX549 fluorescence excitation by 561 nm laser light was three orders of magnitude higher in single-molecule imaging experiments (2 kW/cm^2). These data suggest that an increase in 561 nm photon flux is able to activate the iLID optogenetic response.

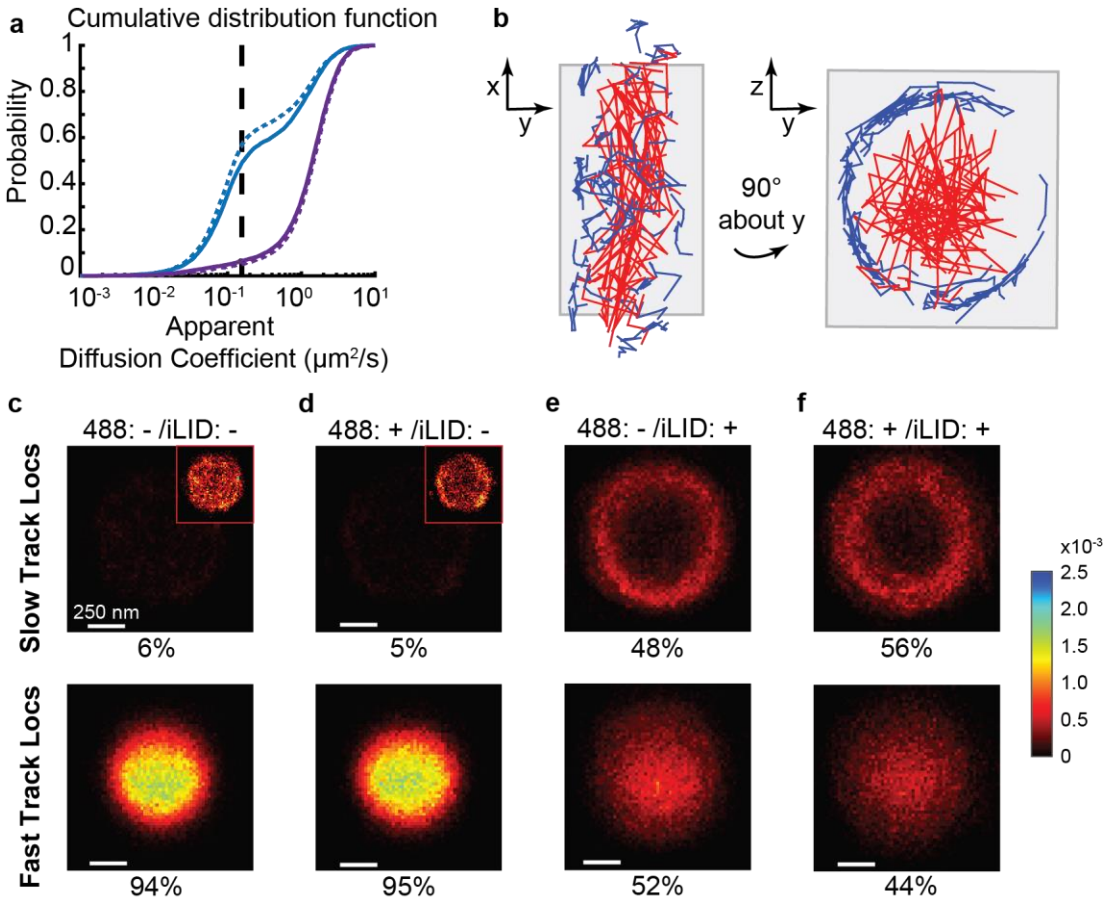

Figure 2. 3D single-molecule tracking data show SspB:iLID interaction prior to 488 nm illumination (a) Apparent diffusion coefficient distributions of $SspB_{nano}$ in the absence (purple, solid line, N = 11,523 tracks, 120 cells) and presence (blue, solid line, N = 8,542 tracks, 78 cells) of MA-iLID. Illumination with 488 nm light marginally increases the population of slowly diffusing $SspB_{nano}$ in MA-iLID expressing cells (blue, dashed line, N = 6,360 tracks, 88 cells), but not in cells which do not express MA-iLID (purple, dashed line, N = 9,922 tracks, 94 cells).

Vertical dashed line indicates threshold used to distinguish fast diffusers ($D^* > 0.15$ μm^2/s) from slow diffusers ($D^* < 0.15$ μm^2/s) **(b)** Single-molecule trajectories in a representative cell expressing MA-iLID, after illumination with 488 nm light. Left: top view. Right: *en face* cross sectional view. Slowly diffusing molecules (blue) clearly localize to the periphery of the cell and diffuse laterally along the membrane, while fast diffusing molecules (red) localize predominately to the cytosol and diffuse in 3D. **(c-f)** 2D histograms of localizations from slow and fast trajectories within the population of cells imaged. Histograms recapitulate trends observed in panel b. Bin size 20 nm x 20 nm. Each histogram is normalized to the total number of molecules observed in that experiment. Inset: rescaled (unnormalized) histograms, shown for clarity.

Single-molecule tracking of SspB mutants further indicate activation of iLID optogenetic response by high intensity 561 nm light.

To decrease the amount of iLID-bound SspB prior to 488 nm illumination, we made a series of previously characterized mutations to SspB[41,42]. These mutant versions of SspB, termed $SspB_{micro}$ and $SspB_{milli}$, have decreased binding affinity for the iLID protein. When we tracked single $SspB_{micro}$ and $SspB_{milli}$ proteins in living cells, we indeed observed a decrease in the fraction of slow diffusers near the cell membrane prior to 488 nm light illumination (**Figure 3a-c**). We found that 31% of $SspB_{micro}$ proteins were iLID-associated, while iLID-associated $SspB_{milli}$ comprised only 6% of the population. Upon 488 nm light illumination, the membrane-proximal, slow-diffusing fractions increased to 45% and 7%, respectively (**Figure 3b** and **c**). The magnitude of the optogenetic response thus differs between the mutants, with $SspB_{micro}$ showing the largest response, under otherwise identical experimental conditions. Diffraction-limited images of $SspB_{micro}$ and $SspB_{milli}$ recapitulate this trend (**SI Figure 3**). Previous work has also shown that the $SspB_{milli}$:iLID interaction is only minimally affected by blue light, as judged based on $SspB_{milli}$ localization to iLID-labeled organelles in HeLa cells[55].

The reported dissociation constants for the three abovementioned SspB mutants differ by six orders of magnitude. The data reported above was collected at the same expression levels for

each interacting protein components. $SspB_{nano}$ may thus saturate the available binding sites at the membrane at the expression level used. Consequently, a large increase in binding upon 488 nm illumination is not observed. At the other extreme, $SspB_{milli}$ may require a much higher number of binding sites to observe binding both before and after 488 nm illumination due to its inherently low affinity for the iLID protein. The comparatively larger optogenetic response observed for $SspB_{micro}$ suggests that the concentration of each interacting parter is better-matched to the dissociation constant for this mutant.

To test this model, we titrated the amount of MA-iLID, while keeping the expression level of $SspB_{micro}$ constant. To estimate the concentration of MA-iLID expressed at each L-arabinose induction concentration, we performed a calibration experiment in which we expressed MA-mCherry-iLID under the same promoter. The number of MA-mCherry-iLID proteins was estimated by dividing the intial fluorescence intensity of each cell by the average intensity of a single mCherry protein. Uninduced cells still expressed MA-mCherry-iLID at a concentration of ~90 nM due to leaky expression from the arabinose promoter (**SI Figure 4**). At the maxium inducer concetration used (13.3 mM), the MA-mCherry-iLID reached a concentration of ~510 nM. For the following analyses, we assume that MA-mCherry-iLID and MA-iLID are expressed at the same level for a given L-arabinose concentration.

Decreasing the concentration of MA-iLID, decreases the fraction of iLID-associated $SspB_{micro}$. At the lowest MA-iLID concentration, $SspB_{micro}$ does not show an appreciable population fraction of slowly diffusing, membrane-proximal molecules both before and after 488 nm illumination (**Figure 3d**). At the highest concentration of MA-iLID , we estimate that 48% of $SspB_{micro}$ is iLID-associated. It is possible that this fraction could be augemented by further increasing the expression level of MA-iLID. However, we found that high expression of MA-

mCherry-iLID leads to an increase in fluorescent foci formation, most often at the cell pole (**SI Figure 5a**). Fluorescent foci formation can be indicative of protein overexpression and subsequent aggregation and/or formation of inclusion bodies[56,57]. These processes do not necessarily interfere with protein folding and function[56,57]. Indeed, we observe fluorescent foci formation in the MA-mCherry-iLID data, but not to the same extent in the $SspB_{micro}$-Halo data (**SI Figure 5b**). These observations suggest that mCherry remains correctly folded and functional within the MA-mCherry-iLID construct, though the iLID protein within the fluorescent foci may not be functional or available for interactions with SspB. Due to the significant increase in fluorescent foci formation, we did not explore higher expression levels of MA-iLID.

Titration of MA-iLID expression allowed us to estimate the dissociation constant K_D of the $SspB_{micro}$:MA-iLID interaction in living cells. Because we observe 48% association of $SspB_{micro}$ at 507 nM MA-iLID, we estimate that the K_D is approximately 510 nM before 488 nm illumination. This value is about 100x smaller than K_D reported in *in vitro* fluorescence polarization assays in unactivated conditions[41]. However, as we argued above, the high intensity 561 nm excitation light activates the iLID optogentic response. Therefore, it is more appropriate to compare results under activated conditions to the fluorescence polarization data. Indeed, the reported *in vitro* K_D is about 800 nM,[41] which is within a factor of two the K_D value we estimate in living cells. Further, we observe ~45% association of $SspB_{micro}$ at ~260 nM MA-iLID in activated conditions, which represents an approximately 2-fold increase in affinity upon 488 nm illumination. The reported dynamic range derived from *in vitro* fluorescence polarization assays is reported to be a 58 fold change in binding affinity due to activation of the system. However, we note that proteins reconstituted in lipid bilayers show a shortened dynamic range of binding affinity, observing a 2.7-fold change in affinity upon iLID-activation[58,59]. Together, these results suggest that proximity to

the membrane, and the steric hindrance imposed by it may affect the dynamics of the SspB:iLID interaction.

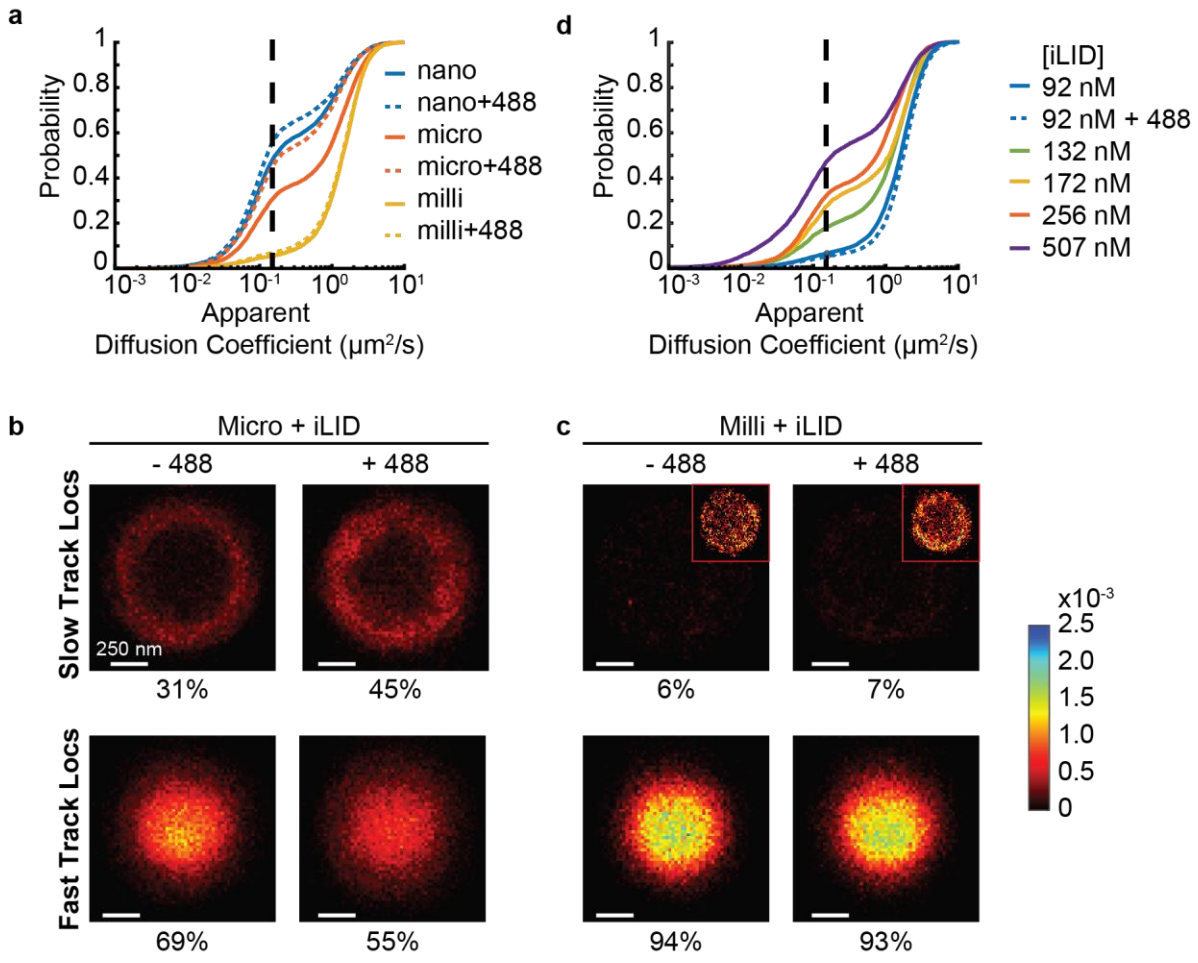

Figure 3. Affinity of the SspB:iLID interaction determines the fraction of iLID-associated SspB observed in single-molecule tracking experiments. (a) Apparent diffusion coefficient distributions for three SspB mutants. The lowest affinity mutant, $SspB_{milli}$ (solid, yellow line, N = 4246 tracks, 65 cells) displays the highest population fraction of fast, cytosolic diffusion prior to 488 nm illumination, followed by $SspB_{micro}$ (solid, orange line, N = 7,738 tracks, 97 cells) and $SspB_{nano}$ (solid, blue line, N = 8,542 tracks, 78 cells). Activation of these systems with 488 nm illumination (dashed line distributions) shifts each mutant proteins's distribution towards larger fractoins of slow diffusing molecules due to MA-iLID association. **(b)** 2D cross-sectional histograms of $SspB_{micro}$ trajectories indicate MA-iLID association at the membrane increases in frequency upon 488 nm illumination (N = 6,491 tracks, 77 cells). Each histogram is normalized to the total number of molecules observed in that experiment. Inset: rescaled (unnormalized) histograms, shown for clarity. **(c)** 2D cross-sectional histograms of $SspB_{milli}$ trajectories indicates

small, but qualitatively discernable MA-iLID association after 488 nm illumination (N = 5243 tracks, 99 cells). **(d)** Apparent diffusion coefficient distribution of $SspB_{micro}$ as a function of MA-iLID expression level. Higher MA-iLID expression levels lead to increased population fractions of slow, membrane-proximal diffusion of $SspB_{micro}$ (see also **SI Figure 4** and **6**).

Cumulative displacement analysis identifies state-switching events in full-length trajectories

Having quantified the dissociation constant of the iLID:SspB interaction, we next sought to determine the kinetics of this interaction. Previous analyses were performed on trajectories which were shortened to contain at most 10 displacements, to prevent averaging over multiple states. Because our data sets contained many long trajectories, we reasoned that some of these trajectories may contain information about the length of time a single SspB protein remains bound to an MA-iLID protein at the membrane. To assess the diffusive behavior over the course of a trajectory, we first calculated the cumulative displacement of each single-molecule over time **(Figure 4a** and **4b**, see methods). These data show a clear separation for fast cytosolic diffusion and slow, membrane-associated diffusion. Because of the clear distinction, we decided that analysis cumulative displacements could be used to differentiate states within single trajectories. To estimate the diffusion coefficients that describe motion in each state, we simulated cytosolic and membrane-bound diffusion at different diffusion rates. We found that the cumulative displacement over time of single-molecule trajectories simulated at 5.5 $\mu m^2/s$ in the cytosol and 0.2 $\mu m^2/s$ at the membrane best matched the experimentally measured cumulative displacement data. These values were then used as references for subsequent analysis.

To identify state switching events within trajectories, we employed the workflow outlined in Figure 4a and c. Briefly, the cumulative displacements of small segments within trajectories were designated as fast diffusion or slow diffusion using a threshold corresponding to D = 1.75

μm^2/s. This threshold was chosen to match the upper-limit of the displacement sizes used in the membrane-bound simulation at 0.2 μm^2/s. Trajectories which exhibited subsequent fast-slow-fast diffusive states were ranked by evaluating the similarity of experimental slope of cumulative displacement data to the abovementioned simulated slopes of cumulative displacement data corresponding to D = 5.5 μm^2/s and 0.2 μm^2/s (**Figure 4d**). We further verified that the best scoring trajectories indeed exhibited slow-diffusing segments at the membrane, and fast-diffusing segments in the cytosol. The resulting subset of trajectories was then used to calculate t_{bound} (**Figure 4e**). As a control, we performed the same analysis for SspB trajectories in the absence of MA-iLID, and, as expected, did not identify clear state switching signatures.

In the presence of 256 nM MA-iLID, $SspB_{micro}$ and $SspB_{nano}$ exhibit similar bound times independent of 488 nm illumination (median = 300 and 350 ms, respectively) while $SspB_{milli}$ displayed comparatively shorter binding times (median = 175 ms) (**Figure 4e**). Thus, the measurements of t_{bound} made in this manner do not show a trend that clearly correlates with each SspB mutant's affinity for the iLID protein or with photoactivation of iLID. Trajectories which were identified as acceptable for residence time measurements were rare (<1% or less of the total number of trajectories analyzed). This low number stands in stark contrast to the much larger fraction of molecules which remained iLID-bound for the duration of the trajectory which matched the trend observed in the analyses of apparent diffusion coefficients (**SI Figure 7**, **Figures 2 and 3**). The length of the trajectories of fully-bound molecules ranges from 0.3 seconds up to 3 seconds (longest observed trajectory – **Figure 4b**). The long lengths of these trajectories (which are terminated by fluorophore photobleaching) suggest that $SspB_{micro}$ proteins can remain iLID-bound for much longer than the median time scales estimated for t_{bound}. Previously published data estimates the dissociation half-life of $SspB_{nano}$ and $SspB_{micro}$ with iLID to occur on the order of

minutes[58,59]. Thus, single-molecule trajectories are not long enough to capture both binding and unbinding events of stable SspB:iLID interactions. These results suggest that short time scale interactions that we capture are representative of a transient binding mode(s) which is(are) not reflective of stable SspB:iLID binding.

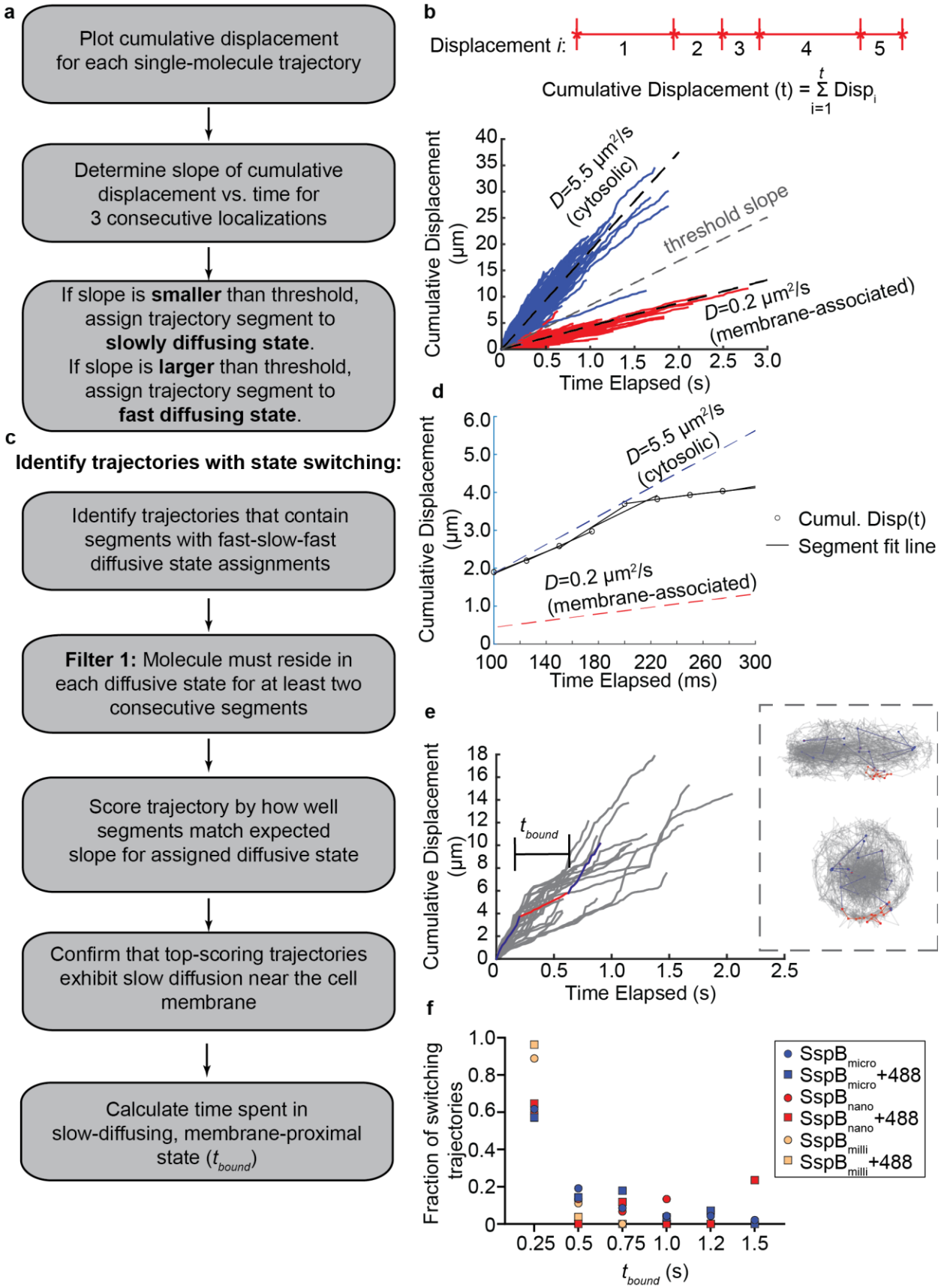
a
Plot cumulative displacement for each single-molecule trajectory
Determine slope of cumulative displacement vs. time for 3 consecutive localizations
If slope is **smaller** than threshold, assign trajectory segment to **slowly diffusing state**.
If slope is **larger** than threshold, assign trajectory segment to **fast diffusing state**.
b
Displacement i:
1
2
3
4
5
Cumulative Displacement (t) = Σ Disp_i
Cumulative Displacement (µm)
Time Elapsed (s)
D=5.5 µm²/s (cytosolic)
threshold slope
D=0.2 µm²/s (membrane-associated)
c
Identify trajectories with state switching:
Identify trajectories that contain segments with fast-slow-fast diffusive state assignments
Filter 1: Molecule must reside in each diffusive state for at least two consecutive segments
Score trajectory by how well segments match expected slope for assigned diffusive state
Confirm that top-scoring trajectories exhibit slow diffusion near the cell membrane
Calculate time spent in slow-diffusing, membrane-proximal state (t_bound)
d
Cumulative Displacement (µm)
Time Elapsed (ms)
D=5.5 µm²/s (cytosolic)
D=0.2 µm²/s (membrane-associated)
Cumul. Disp(t)
Segment fit line
e
Cumulative Displacement (µm)
Time Elapsed (s)
t_bound
f
Fraction of switching trajectories
t_bound (s)
SspB_micro
SspB_micro+488
SspB_nano
SspB_nano+488
SspB_milli
SspB_milli+488

389

Figure 4. Cumulative displacement analysis identifies state-switching events in single-molecule trajectories. (a) Workflow of cumulative displacement analysis to distinguish fast, cytosolic diffusing molecules from slow, membrane-associated molecules. **(b)** Top panel: Schematic of displacement data transformed into a 1D trajectory to illustrate displacement size over time. The cumulative displacement is the sum of all displacements up to a given time point, *t*. Bottom panel: Cumulative displacement over time for $SspB_{micro}$ trajectories collected in MA-iLID expressing cells (256 nM) in unactivated conditions. A threshold slope corresponding to D = 1.75 $\mu m^2/s$ was used to distinguish fast diffusing molecules (blue) from slow diffusing molecules (red). Simulated trajectories in the cytosol at 5.5 $\mu m^2/s$ and in the membrane at 0.2 $\mu m^2/s$ recapitulated experimental cumulative displacement slopes and were used as reference slopes in the following steps. **(c)** Workflow used to identify trajectories with state-switching (see text for details). **(d)** Example of a $SspB_{micro}$ partial trajectory which exhibits state-switching. Three consecutive cumulative displacements are fit to a line, and the slope is compared to the threshold slope to classify the trajectory segment as cytosolic or membrane-bound. The slope of the segment is then compared to the reference slope for cytosolic diffusion or membrane diffusion depending on the state assignment, and scored by how closely they match. Trajectories with at least 2 consecutive segments in cytosolic and then membrane-associated states (or vice versa) are categorized as state-switching and used for later analysis. **(e)** Cumulative displacements over time of trajectories which show state transitions of fast-slow-fast. Trajectory localization of example fast(blue)-slow(red)-fast(blue) state-switching cumulative displacement plotted to highlight state transition at the membrane of the cell. Time spent in bound state (red portion of trajectory) is integrated to calculate the residence time t_{bound}. **(f)** Histogram of residence times of SspB affinity mutants (bin size = 250 ms) indicate that transient binding modes to MA-iLID do not exhibit residence times that are dependent on the affinity of the SspB:iLID interaction.

CONCLUSIONS

Here, we provide a quantitative analysis of the iLID optogenetic system in live K12 *E. coli* cells using 2D diffraction-limited imaging and 3D single-molecule tracking. We show that the iLID system enables efficient optogenetic manipulation of protein spatial distributions when used in conjunction with diffraction-limited imaging. Single-molecule tracking data acquired using high intensity 561 nm laser excitation leads to a substantial amount of SspB:iLID interaction even in the absence of optogenetic activation at 488 nm. This suggests that increased photon flux is somehow able to activate the iLID optogenetic response, even though the LOV2 domain absorption spectra suggest that wavelengths greater than 500 nm should not be absorbed[54]. This conclusion is consistent with our observation that even low intensity 514 nm illumination is able

to increase the SspB:iLID interaction. However, published LOV2 domain absorption spectra were collected using purified proteins[54]. It is possible that cellular contents, proximity to the membrane and imposed steric hindrance results in a shift in iLID conformational dynamics and thus a change in interaction with SspB. A similar effect has been seen in other model systems utilizing the iLID:SspB interaction[58,59]. This may explain the rare, transient binding events that we measured in single- molecule trajectory analyses. Our results highlight the importance of calibrating the effects of illumination conditions and cellular environment when the iLID system, or any optogenetic system, is used to modulate an SspB-tagged protein's spatial distribution.

A notable advantage of optogenetic systems, such as iLIDs, is that dimerization can be induced in real time using light. Optically-induced dimerization can be enabled much faster than chemically induced dimerization, which are diffusion-limited. We aim to combine optogenetic perturbation with single-molecule tracking to deplete cytosolic diffusive states that have been assigned to hetero-oligomeric protein complexes based on control experiments in genetically perturbed backgrounds. Although a pre-activated system dampens the magnitude of the optogenetic response that can be observed, highly sampled distributions obtained from tens of thousands of single-molecule trajectories, may allow for the observation of cytosolic diffusive states depletion with sufficient statistical power. Additionally, titration of protein expression can be used to incrementally sequester proteins of interest. Another alternative might be to use far-red excitable fluorophores for single-molecule tracking. Based on the trends observed here we speculate that high intensity red and far-red light illumination will not activate the iLID system. Thus, single-molecule localization and tracking microscopy with red and far-red fluorophores could enable observations of large optogenetic responses, similar to those observed in diffraction-limited imaging.

METHODS:

Bacterial strains and plasmids

Escherichia coli K12 (MG1655) strains were generated by introducing pACYC and pBAD vectors containing genes encoding the cytosolic prey protein, SspB, and the membrane-anchored bait protein, iLID, respectively. pACYC $SspB_{nano}$-Halo was derived from pACYC $SspB_{nano}$-mCherry (pFL109) which was a gift from Andreas Diepold. The construct was modified by removing mCherry from the plasmid via restriction digest and the *halo* coding sequence was ligated in its place, using XhoI and SalI cut sites. The plasmid containing the bait protein, pBad FLAG-iLID (pFL108), also a gift from the Diepold lab, was transformed into bacteria without any further modification.

Cell culture

E. coli cultures were inoculated from a freezer stock and grown overnight in LB media at 37° C and shaking at 225 rpm. Strains expressing from the pACYC and pBAD plasmids were grown in 30 µg/mL chloramphenicol and 100 µg/mL ampicillin, respectively. Overnight cultures were diluted to an OD_{600} of 0.05 in M9 minimal media and incubated at 37° C. Strains containing the pBAD plasmid were induced with 5.33 mM L-arabinose after 2 hours unless indicated otherwise. After an additional 1.5 hours of growth, 1.5 mL of cell culture was aliquoted and stained with 1.5 µL of 500 µM JFX-549 dye. The cell suspension mixture was incubated at 37° C for 30 minutes and then washed four times with M9 minimal media. Cell pellets were resuspended in a final volume of 10 µL for use in imaging experiments.

E. coli cells were transformed with plasmids via heat shock of chemically competent cells. Transformed cells were selected for by growing on LB agar plates containing chloramphenicol,

ampicillin (100 µg/mL), or a combination of both for co-expressing strains. Transformants were screened by performing a Western blot for FLAG or Halo proteins in pBAD and pACYC-containing strains, respectively. Strains which showed a clear band in Western blot experiments were used to make freezer stocks containing 15% glycerol.

Optical setup

Imaging of cells was performed on a home-built inverted fluorescence microscope as described previously[24]. The microscope was modified for use in optogenetics experiments by incorporation of an additional 488nm laser line (Coherent Genesis) for activation of the iLID system. Fluorescence images were collected in the "red" channel of the imaging system.

Epifluorescence imaging

Stained cells were mounted on a #1.5 coverslips (VWR) and immobilized using 1.5% agarose pad prepared in M9 minimal media. Halo-conjugated JFX549 was excited using 561 nm laser light at ~1 W/cm^2. Images were acquired at 5 frames/sec for 40 seconds pre- and post-activation of the iLID optogenetics system. The iLID optogenetic system was activated using 488 nm laser light at ~4 mW/cm^2 continuously for 2 minutes prior to and then also during acquisition of post-activation images. Epifluorescence images shown in the figures represent averages of these image sequences. Brightfield images were acquired of the same field-of-view by illuminating cells with an LED, and taking a single 25 ms exposure.

SSIM analysis of Diffraction-limited images

Pre- and post- activation images were background subtracted. Outlines of cells were derived by using OUFTI[60] on inverted color to create a binary mask such that each cell was compared to itself before and after activation. The built-in Matlab (The MathWorks, Inc, Natick, Massachusetts)

function ssim() was applied to the masked images with equal weighting of the comparison metrics, luminance, structure, and contrast, to assess the degree of image similarity. Cells with abnormal morphology (based on the associated brightfield image) were excluded from the analysis. Multiple fields of view were acquired for each condition, and the experiments were replicated twice.

Super-resolution fluorescence imaging

Fluorescent fiducial markers (Invitrogen) were added to cell suspensions and the cell suspension was then mounted on #1.5 glass coverslips. Cells were immobilized using solidified pads of 1.5% agarose in M9 minimal media. Halo-conjugated JFX-549 was excited into the blinking state by 561 nm laser light at ~2 kW/cm^2 at the sample. Images were acquired at 40 frames/sec in the presence or absence optogenetic activating 488 nm light. Cells were activated using 488 nm laser light at ~4 mW/cm^2 continuously for 2 minutes prior to and during acquisition of post-activation images.

Data Processing

Raw data was processed in Matlab (The MathWorks, Inc, Natick, Massachusetts) using a modified version of easy-DHPSF software[24,61]. Fluorescent fiducial markers were used for sample drift correction. Single-molecule localizations were registered to phase contrast images using a two-step affine transformation in MATLAB as previously described[24]. Localizations outside of cells were discarded from further analysis using axial bounds and OUFTI-derived cell outlines which were generated from phase contrast images, as described above.

Single-molecule tracking analysis

To derive single-molecule displacements, localizations in subsequent frames were linked into trajectories. A maximum linking distance of 2.5 um was used for linking analysis, and multiple

localizations which were present at the same time within a single cell were discarded to prevent misassignment of molecules.

The Mean Squared Displacement (MSD) for each trajectory was calculated using

$$\mathrm{MSD} = \frac{1}{(N-1)}\sum_{n=2}^{N}(x_n - x_{n-1})^2$$

where x is the 3D position at timepoint n, including up to 11 timepoints for calculating the mean over 10 displacements. The remainder of the trajectory was not used in the MSD analysis to ensure multiple diffusive states were not averaged over. The MSD measurement was then used to calculate the apparent diffusion coefficient (D^*) according to:

$$D^* = \frac{\mathrm{MSD}}{2 \cdot m \cdot \Delta t}$$

Where m is the dimensionality of the measurement (m=3 for the 3D trajectories reported here), and Δt is the camera exposure time used for imaging (Δt=25 ms under our conditions).

2D-cross section projection analysis

The vector describing the central axis of each cell was determined using the cell outline generated from OUFTI. The outline was segmented into sections along the cell length, and localizations from trajectories in each section were projected onto a 2D plane. The position of the central cell axis was adjusted to match the centroid of all localizations within the section. Positions of localizations from each cell were scaled to match the mean cell radius and mean cell length which was calculated from OUFTI outlines. The trajectories were classified as slow or fast diffusing using the threshold

$D^* = 0.15$ μm^2/s which was determined by identifying a transition point from the first major change in slope in the CDF plot of apparent diffusion coefficients of data containing both iLID-associated and cytosolic diffusion (**Figure 1**).

Determination of residence times - t_{bound}

To identify diffusive state transitions in single-molecule trajectories, we developed a workflow to analyze displacement data over time (**Figure 4a and c**). First, we plotted the additive, or cumulative displacement (CD) as a function of time elapsed according to:

$$\mathrm{CD}(t) = \sum_{t=1}^{N} \sqrt{(x_t - x_{t-1})^2}$$

where x is the 3D position at timepoint t. The CD was calculated for each displacement, for the full trajectory length (N).

The instantaneous rate of displacement was estimated by finding the slope within a small, sliding window containing 3 displacements for the full length of the trajectory (**Figure 4d**). The size of the sliding window was chosen to be small enough such that switching events were not excessively averaged over, while being large enough to be somewhat insensitive to displacement size fluctuations. Each segment of the trajectory was then classified as bound or free by calculating its slope and comparing it to a threshold, which was chosen to match the upper-limit of the displacement sizes used in the membrane-bound simulation at 0.2 μm^2/s. Trajectories which contained consecutive segments of fast-slow-fast state assignments were used for further analysis because of the presence of an internal bound state. To be considered for analysis, the molecule must reside in each state for at least 2 segments (4 displacements) of the trajectory to ensure that the identified state change was a true diffusive state change and not due to random fluctuation.

Each switching trajectory was ascribed a score (TS) by how well the slope of trajectory segments matched simulated diffusion coefficient slopes derived for freely diffusing, cytosolic and membrane-bound molecules:

$$TS = \frac{1}{N_{seg} - 2} \sum_{i=1}^{N_{seg}} e^{-|m_i - m_s|}$$

where m_i is the slope fit to the experimental trajectory segment, and m_s is the slope derived from free cytosolic or membrane-bound simulated data, depending on the state assigned to the trajectory segment. N_{seg} refers to the number of segments in the trajectory. Switching trajectories were ranked by their TS, and the top-scoring trajectories (TS>~0.16) were inspected individually to verify that switching events occurred at the membrane of the cell. The residence time (t_{bound}) of bound molecules in these switching trajectories was calculated by determine the number of displacements the molecule was assigned to the bound state.

3D single-molecule trajectory simulation

Cytosolic trajectories were simulated as described previously.[23,24] Briefly, Monte Carlo simulations of Brownian motion at 5.5 $\mu m^2/s$ were confined to the volume of a cylinder matching the dimensions of K12 *E. coli* (radius = 0.5 µm, length = 2.5 µm). Initial positions of molecules were randomly selected to uniformly fill the volume of the cell, and subsequent positions in the trajectory were selected at 100 ns intervals for a total of 125 ms. We simulated noisy, motion-blurred images of the single-molecule trajectories, integrating images over subsequent 25 ms time intervals, to match experimental camera exposure times for a total of 6 images per single-molecule track. We simulated 1000 such trajectories. To best match data derived from experimental

conditions, we analyzed the simulated images of trajectories in the same way described for experimental localization and tracking. Easy-DHPSF software was used to analyze the images and detect single-molecule localizations.

Membrane-bound trajectories were simulated for molecules diffusing at 0.2 $\mu m^2/s$. Initial positions were randomly chosen on the surface of a spherocylinder matching the dimensions of K12 *E. coli* (radius = 0.5 µm, length = 2.5 µm). Monte Carlo simulations of molecular motion were confined to the surface of the spherocylinder by translating displacements to changes in lateral position and elevation angle on the cylindrical surface or elevation and azimuthal angle on the hemispherical surface, such that the distance from the cell axis is always equal to the radius of the cell. Positions were updated at 100 ns intervals for a total of 125 ms. Images were generated and analyzed as described in the previous paragraph.

2D diffraction-limited image simulation

Trajectories of cytosolic and membrane-associated diffusing molecules were simulated as described above with the following modifications to match diffraction-limited imaging conditions. Positions were sampled every 1 µs for a total of 1.2 seconds. Molecule positions were sampled ever 200 ms, resulting in 6 localization positions (macro-positions) per track.

The three dimensional molecule macro-positions were used to generate conventional diffraction-limited 2D point-spread functions of isotropic emitters using a vectorial light propagation model.[62] We modified the algorithm to omit the double helix phase mask and optical aberrations. In the simulation, the nominal focal plane was positioned at the center of the cell. A total of 10,000 trajectories were simulated for both cytosolic and membrane-bound molecules, providing 60,000 total emitter positions in each condition. Images obtained for each emitter were added to attain the

total image. To attain mixed population images, trajectories were chosen at random from the total simulated trajectory population to reflect the specified membrane-associated molecule fraction.

REFERENCES:

1 Achimovich, A. M., Ai, H. & Gahlmann, A. Enabling technologies in super-resolution fluorescence microscopy: reporters, labeling, and methods of measurement. *Current Opinion in Structural Biology* **58**, 224-232, doi:https://doi.org/10.1016/j.sbi.2019.05.001 (2019).

2 Aaron, J. S., Taylor, A. B. & Chew, T.-L. Image co-localization – co-occurrence versus correlation. *Journal of Cell Science* **131**, jcs211847, doi:10.1242/jcs.211847 (2018).

3 Szymborska, A. *et al.* Nuclear Pore Scaffold Structure Analyzed by Super-Resolution Microscopy and Particle Averaging. *Science* **341**, 655-658, doi:10.1126/science.1240672 (2013).

4 Sieben, C., Banterle, N., Douglass, K. M., Gönczy, P. & Manley, S. Multicolor single-particle reconstruction of protein complexes. *Nature Methods* **15**, 777-780, doi:10.1038/s41592-018-0140-x (2018).

5 Thevathasan, J. V. *et al.* Nuclear pores as versatile reference standards for quantitative superresolution microscopy. *Nature Methods* **16**, 1045-1053, doi:10.1038/s41592-019-0574-9 (2019).

6 Malkusch, S. *et al.* Coordinate-based colocalization analysis of single-molecule localization microscopy data. *Histochemistry and cell biology*, doi:10.1007/s00418-011-0880-5 (2011).

619 7 Larson, J. D., Rodgers, M. L. & Hoskins, A. A. Visualizing cellular machines with
620 colocalization single molecule microscopy. *Chem. Soc. Rev.* **43**, 1189-1200,
621 doi:10.1039/c3cs60208g (2014).
622 8 Levet, F. *et al.* A tessellation-based colocalization analysis approach for single-
623 molecule localization microscopy. *Nature communications* **10**, doi:10.1038/s41467-
624 019-10007-4 (2019).
625 9 Magde, D., Elson, E. & Webb, W. W. Thermodynamic Fluctuations in a Reacting
626 System—Measurement by Fluorescence Correlation Spectroscopy. *Phys. Rev. Lett.*
627 **29**, 705-708, doi:10.1103/physrevlett.29.705 (1972).
628 10 Axelrod, D. K., D. E.; Schlessinger J.; Elson, E.; Webb, W.W. Mobility measurement by
629 analysis of fluorescence photobleaching recovery kinetics. *Biophysical journal* **16**,
630 1055-1069, doi:https://doi.org/10.1016/S0006-3495(76)85755-4 (1976).
631 11 Koppel, D. E. A., D.; Schlessinger, J.; Elson, E. L.; Webb, W. W. . Dynamics of
632 fluorescence marker concentration as a probe of mobility. *Biophysical journal* **16**,
633 1315-1329 (1976).
634 12 Wachsmuth, M. Molecular diffusion and binding analyzed with FRAP. *Protoplasma*
635 **251**, 373-382, doi:10.1007/s00709-013-0604-x (2014).
636 13 Muller, K. P. *et al.* Multiscale analysis of dynamics and interactions of
637 heterochromatin protein 1 by fluorescence fluctuation microscopy. *Biophysical*
638 *journal* **97**, 2876-2885, doi:10.1016/j.bpj.2009.08.057 (2009).
639 14 Zeug, A., Woehler, A., Neher, E. & Evgeni. Quantitative Intensity-Based FRET
640 Approaches—A Comparative Snapshot. *Biophysical journal* **103**, 1821-1827,
641 doi:10.1016/j.bpj.2012.09.031 (2012).

642 15 Forster, T. Energiewanderung und fluoreszenz. *Naturwissenschaften* **33**, 166-175
643 (1946).
644 16 Elf, J. & Barkefors, I. Single-Molecule Kinetics in Living Cells. *Annual Review of*
645 *Biochemistry* **88**, 635-659, doi:10.1146/annurev-biochem-013118-110801 (2019).
646 17 Karslake, J. D. *et al.* SMAUG: Analyzing single-molecule tracks with nonparametric
647 Bayesian statistics. *Methods* **193**, 16-26, doi:10.1016/j.ymeth.2020.03.008 (2021).
648 18 Hansen, A. S. *et al.* Robust model-based analysis of single-particle tracking
649 experiments with Spot-On. *Elife* **7**, doi:10.7554/eLife.33125 (2018).
650 19 Persson, F., Lindén, M., Unoson, C. & Elf, J. Extracting intracellular diffusive states
651 and transition rates from single-molecule tracking data. *Nature Methods* **10**, 265-
652 269, doi:10.1038/nmeth.2367 (2013).
653 20 Monnier, N. *et al.* Inferring transient particle transport dynamics in live cells. *Nat*
654 *Methods* **12**, 838-840, doi:10.1038/nmeth.3483 (2015).
655 21 Chen, T. Y. *et al.* Quantifying Multistate Cytoplasmic Molecular Diffusion in Bacterial
656 Cells via Inverse Transform of Confined Displacement Distribution. *The journal of*
657 *physical chemistry. B* **119**, 14451-14459, doi:10.1021/acs.jpcb.5b08654 (2015).
658 22 Michalet, X. & Berglund, A. J. Optimal diffusion coefficient estimation in single-
659 particle tracking. *Physical Review E* **85**, doi:10.1103/PhysRevE.85.061916 (2012).
660 23 Rocha, J., Corbitt, J., Yan, T., Richardson, C. & Gahlmann, A. Resolving Cytosolic
661 Diffusive States in Bacteria by Single-Molecule Tracking. *Biophysical journal* **116**,
662 1970-1983, doi:https://doi.org/10.1016/j.bpj.2019.03.039 (2019).

663 24 Rocha, J. M. *et al.* Single-molecule tracking in live Yersinia enterocolitica reveals
664 distinct cytosolic complexes of injectisome subunits. *Integrative Biology* **10**, 502-
665 515, doi:10.1039/c8ib00075a (2018).
666 25 Prindle, J. R., Rocha, J., Wang, Y., Diepold, A. & Gahlmann, A. Distinct complexes
667 containing the cytosolic type III secretion system ATPase resolved by 3D single-
668 molecule tracking in live Yersinia enterocolitica. *bioRxiv*,
669 2022.2004.2025.488798, doi:10.1101/2022.04.25.488798 (2022).
670 26 Gahlmann, A. & Moerner, W. E. Exploring bacterial cell biology with single-molecule
671 tracking and super-resolution imaging. *Nature Reviews Microbiology* **12**, 9-22,
672 doi:10.1038/nrmicro3154 (2014).
673 27 Au - Uphoff, S., Au - Sherratt, D. J. & Au - Kapanidis, A. N. Visualizing Protein-DNA
674 Interactions in Live Bacterial Cells Using Photoactivated Single-molecule Tracking.
675 *JoVE*, e51177, doi:doi:10.3791/51177 (2014).
676 28 Badrinarayanan, A., Reyes-Lamothe, R., Uphoff, S., Leake, M. C. & Sherratt, D. J. *In*
677 *Vivo* Architecture and Action of Bacterial Structural Maintenance of Chromosome
678 Proteins. *Science* **338**, 528-531, doi:10.1126/science.1227126 (2012).
679 29 Stracy, M. *et al.* Single-molecule imaging of UvrA and UvrB recruitment to DNA
680 lesions in living Escherichia coli. *Nature communications* **7**, 12568,
681 doi:10.1038/ncomms12568 (2016).
682 30 Uphoff, S. *et al.* Stochastic activation of a DNA damage response causes cell-to-cell
683 mutation rate variation. *Science* **351**, 1094-1097, doi:10.1126/science.aac9786
684 (2016).

685 31 Uphoff, S., Reyes-Lamothe, R., Garza de Leon, F., Sherratt, D. J. & Kapanidis, A. N.
686 Single-molecule DNA repair in live bacteria. *Proceedings of the National Academy of*
687 *Sciences of the United States of America* **110**, 8063-8068,
688 doi:10.1073/pnas.1301804110 (2013).
689 32 Liao, Y., Schroeder, J. W., Gao, B., Simmons, L. A. & Biteen, J. S. Single-molecule
690 motions and interactions in live cells reveal target search dynamics in mismatch
691 repair. *Proc Natl Acad Sci U S A* **112**, E6898-6906, doi:10.1073/pnas.1507386112
692 (2015).
693 33 Liao, Y., Li, Y., Schroeder, J. W., Simmons, L. A. & Biteen, J. S. Single-Molecule DNA
694 Polymerase Dynamics at a Bacterial Replisome in Live Cells. *Biophysical journal* **111**,
695 2562-2569, doi:10.1016/j.bpj.2016.11.006 (2016).
696 34 Calkins, A. L. *et al.* Independent Promoter Recognition by TcpP Precedes
697 Cooperative Promoter Activation by TcpP and ToxR. *mBio* **12**, e0221321,
698 doi:10.1128/mBio.02213-21 (2021).
699 35 Li, Y., Schroeder, J. W., Simmons, L. A. & Biteen, J. S. Visualizing bacterial DNA
700 replication and repair with molecular resolution. *Curr Opin Microbiol* **43**, 38-45,
701 doi:10.1016/j.mib.2017.11.009 (2017).
702 36 Li, Y., Chen, Z., Matthews, L. A., Simmons, L. A. & Biteen, J. S. Dynamic Exchange of
703 Two Essential DNA Polymerases during Replication and after Fork Arrest.
704 *Biophysical journal* **116**, 684-693, doi:10.1016/j.bpj.2019.01.008 (2019).
705 37 Peters, J. M. *et al.* A Comprehensive, CRISPR-based Functional Analysis of Essential
706 Genes in Bacteria. *Cell* **165**, 1493-1506, doi:10.1016/j.cell.2016.05.003 (2016).

707 38 Ye, Y.-N., Hua, Z.-G., Huang, J., Rao, N. & Guo, F.-B. CEG: a database of essential gene
708 clusters. *BMC Genomics* **14**, 769, doi:10.1186/1471-2164-14-769 (2013).
709 39 Robinson, M. S. & Hirst, J. Rapid inactivation of proteins by knocksideways. *Curr*
710 *Protoc Cell Biol* **61**, 15 20 11-17, doi:10.1002/0471143030.cb1520s61 (2013).
711 40 Benedetti, L. *et al.* Light-activated protein interaction with high spatial subcellular
712 confinement. *Proc Natl Acad Sci U S A* **115**, E2238-E2245,
713 doi:10.1073/pnas.1713845115 (2018).
714 41 Guntas, G. *et al.* Engineering an improved light-induced dimer (iLID) for controlling
715 the localization and activity of signaling proteins. *Proc Natl Acad Sci U S A* **112**, 112-
716 117, doi:10.1073/pnas.1417910112 (2015).
717 42 Zimmerman, S. P. *et al.* Tuning the Binding Affinities and Reversion Kinetics of a
718 Light Inducible Dimer Allows Control of Transmembrane Protein Localization.
719 *Biochemistry* **55**, 5264-5271, doi:10.1021/acs.biochem.6b00529 (2016).
720 43 Lindner, F., Gahlmann, A. & Diepold, A. Optogenetic control of protein translocation:
721 Protein secretion and translocation into eukaryotic cells with high spatial and
722 temporal resolution by light-controlled activation of the bacterial type III secretion
723 system. European Patent Application 19166308 patent (2019).
724 44 Harper, S. M. Structural Basis of a Phototropin Light Switch. *Science (American*
725 *Association for the Advancement of Science)* **301**, 1541-1544.
726 45 Zayner, J. P., Antoniou, C. & Sosnick, T. R. The Amino-Terminal Helix Modulates
727 Light-Activated Conformational Changes in AsLOV2. *J. Mol. Biol.* **419**, 61-74,
728 doi:10.1016/j.jmb.2012.02.037 (2012).

729 46 Kramer, M. M., Lataster, L., Weber, W. & Radziwill, G. Optogenetic Approaches for
730 the Spatiotemporal Control of Signal Transduction Pathways. *International Journal*
731 *of Molecular Sciences* **22**, 5300, doi:10.3390/ijms22105300 (2021).
732 47 Wittmann, T., Dema, A. & Van Haren, J. Lights, cytoskeleton, action: Optogenetic
733 control of cell dynamics. *Current Opinion in Cell Biology* **66**, 1-10,
734 doi:10.1016/j.ceb.2020.03.003 (2020).
735 48 De Geyter, J., Smets, D., Karamanou, S. & Economou, A. 337-366 (Springer
736 International Publishing, 2019).
737 49 Cline, K. Mechanistic Aspects of Folded Protein Transport by the Twin Arginine
738 Translocase (Tat). *Journal of Biological Chemistry* **290**, 16530-16538,
739 doi:10.1074/jbc.r114.626820 (2015).
740 50 Lindner, F., Milne-Davies, B., Langenfeld, K., Stiewe, T. & Diepold, A. LITESEC-T3SS -
741 Light-controlled protein delivery into eukaryotic cells with high spatial and
742 temporal resolution. *Nature communications* **11**, 2381, doi:10.1038/s41467-020-
743 16169-w (2020).
744 51 Grimm, J. B. *et al.* A General Method to Improve Fluorophores Using Deuterated
745 Auxochromes. *JACS Au* **1**, 690-696, doi:10.1021/jacsau.1c00006 (2021).
746 52 Wang, Z., Simoncelli, E. P. & Bovik, A. C. (IEEE, 2003).
747 53 Elf, J. & Barkefors, I. Single-Molecule Kinetics in Living Cells. *Annu Rev Biochem* **88**,
748 635-659, doi:10.1146/annurev-biochem-013118-110801 (2019).
749 54 Swartz, T. E. *et al.* The Photocycle of a Flavin-binding Domain of the Blue Light
750 Photoreceptor Phototropin. *Journal of Biological Chemistry* **276**, 36493-36500,
751 doi:10.1074/jbc.m103114200 (2001).

752 55 Nijenhuis, W., Van Grinsven, M. M. P. & Kapitein, L. C. An optimized toolbox for the
753 optogenetic control of intracellular transport. *J. Cell Biol.* **219**,
754 doi:10.1083/jcb.201907149 (2020).
755 56 García-Fruitós, E. *et al.* Aggregation as bacterial inclusion bodies does not imply
756 inactivation of enzymes and fluorescent proteins. *Microbial Cell Factories* **4**, 27,
757 doi:10.1186/1475-2859-4-27 (2005).
758 57 Rinas, U. *et al.* Bacterial Inclusion Bodies: Discovering Their Better Half. *Trends in*
759 *Biochemical Sciences* **42**, 726-737, doi:10.1016/j.tibs.2017.01.005 (2017).
760 58 Bartelt, S. M. *et al.* Dynamic blue light-switchable protein patterns on giant
761 unilamellar vesicles. *Chemical communications* **54**, 948-951,
762 doi:10.1039/c7cc08758f (2018).
763 59 Bartelt, S. M., Steinkühler, J., Dimova, R. & Wegner, S. V. Light-Guided Motility of a
764 Minimal Synthetic Cell. *Nano Letters* **18**, 7268-7274,
765 doi:10.1021/acs.nanolett.8b03469 (2018).
766 60 Paintdakhi, A. *et al.* Oufti: An integrated software package for high-accuracy, high-
767 throughput quantitative microscopy analysis. *Molecular microbiology* **99**, 767-777,
768 doi:10.1111/mmi.13264 (2016).
769 61 Lew, M., Von Diezmann, A. R. S. & Moerner, W. E. Easy-DHPSF open-source software
770 for three-dimensional localization of single molecules with precision beyond the
771 optical diffraction limit. *Protoc. Exch.* (2013).
772 62 Yan, T., Richardson, C. J., Zhang, M. & Gahlmann, A. Computational correction of
773 spatially variant optical aberrations in 3D single-molecule localization microscopy.
774 *Optics express* **27**, 12582-12599 (2019).

775